

Tropospheric Rossby Wave Breaking and the SAM

YI-HUI WANG AND GUDRUN MAGNUSDOTTIR

University of California, Irvine, Irvine, California

(Manuscript received 17 August 2010, in final form 23 November 2010)

ABSTRACT

An objective analysis of tropospheric anticyclonic- and cyclonic-breaking Rossby waves is performed for the Southern Hemisphere in austral summer (December–February) of 1979–2009. The climatology of both anticyclonic and cyclonic Rossby wave breaking (RWB) frequency is presented. The frequency of anticyclonic RWB is highest in an extended region of the Eastern Hemisphere on the anticyclonic side of the jet, while that of cyclonic RWB is highest on the cyclonic side of the jet. A composite analysis of anticyclonic and cyclonic RWB shows how they contribute to a positive and negative southern annual mode (SAM) index, respectively. The time series of austral summer anticyclonic RWB occurrence has a trend that closely matches the trend in the SAM index.

Regions of RWB that are significantly correlated with the SAM index are objectively determined. Even though several such regions are identified, only two regions (anticyclonic and cyclonic) covering 17% of the area of the hemisphere are required in a linear regression model of the SAM index. The anticyclonic RWB region is zonally extended at 45°S and explains 78% of the variability of the summer-mean SAM index. The cyclonic region is located at high latitudes somewhat decoupled from the jet, in the longitudinal sector of the Indian Ocean. On synoptic time scales, transitions of the SAM index respond to RWB without time lag.

ENSO cycles present an interesting zonal asymmetry to the distribution of Southern Hemispheric RWB in the central Pacific. Anticyclonic RWB is increased in the tropical/subtropical central Pacific during La Niña compared to El Niño. This increase is related to the strong local decrease in zonal wind. At the same time, anticyclonic RWB outside the central Pacific is increased in frequency poleward and decreased in frequency equatorward of 42°S, corresponding to a positive SAM index.

1. Introduction

The dominant patterns of extratropical climate variability include the North Atlantic Oscillation (NAO, for a restricted longitudinal domain) or northern annular mode (NAM, for a hemispheric domain) in the Northern Hemisphere (NH) and the southern annular mode (SAM) in the Southern Hemisphere (SH). Change in polarity of NAO–NAM and SAM can be interpreted as a meridional shift of the eddy-driven jet, poleward for the positive polarity and equatorward for the negative polarity of the annular modes. These atmospheric modes are mainly driven by relatively short time-scale stochastic processes (on the order of days) (Feldstein 2000; Lorenz and Hartmann 2001) that involve the interaction between eddies and the background flow, for example, Rossby wave breaking (RWB). RWB takes place when potential

vorticity (PV) contours on an isentropic surface are irreversibly and rapidly deformed (McIntyre and Palmer 1983). Depending on the tilted direction of overturning PV contours, RWB is classified into anticyclonic wave breaking or cyclonic wave breaking (Martius et al. 2007; Thorncroft et al. 1993). The two types of RWB have different transport and mixing properties (e.g., Nakamura and Plumb 1994).

A number of studies have found that the NAO is forced by transient eddy momentum fluxes from synoptic RWB. Benedict et al. (2004) found that the life cycle of the NAO was dominated by consecutive synoptic-scale RWB events. Rivière and Orlandi (2007) deduced from the meridional momentum flux that anticyclonic RWB induces the positive polarity of the NAO, while cyclonic RWB induces its negative polarity. Strong and Magnusdottir (2008, hereafter SM08) actually diagnosed anticyclonic and cyclonic RWB and found that in some instances, anticyclonic RWB induces the negative NAM polarity, or negative NAM index (NAMI), and cyclonic RWB induces the positive NAM polarity (NAMI), depending on the latitude of RWB occurrence. Woollings et al. (2008) found that prolonged

Corresponding author address: Yi-Hui Wang, Department of Earth System Science, University of California, Irvine, Irvine, CA 92697-3100.
E-mail: yihuiw@uci.edu

blocking-like PV gradient reversals that sometimes follow RWB over the North Atlantic were more frequent (infrequent) during the negative (positive) polarity of the NAO.

According to SM08, the polarity of the NAM is driven by RWB that takes place in localized areas preferably at the downstream end of the jet maxima. The overall spatial and temporal distribution of RWB in the SH is not known, even though several studies have addressed some parts of this distribution using different methodologies of RWB detection. Berrisford et al. (2007) detected those SH wave-breaking events that lasted longer than four days and were associated with blocking. Hitchman and Huesmann (2007) documented a seasonal climatology of RWB by examining the geometry of specific PV contours on many different isentropic surfaces. But they did not distinguish between the two types of wave breaking. Gong et al. (2010) provide a measure of strength of wave breaking in a zonally average sense. To our knowledge, a Southern Hemispheric view of tropospheric anticyclonic and cyclonic RWB spatial distribution has not been examined to date.¹

Previous studies (e.g., Lorenz and Hartmann 2001; Codron 2005 and references therein) conclude that momentum fluxes of high-frequency eddies respond to the movement of a midlatitude jet and then create zonal wind anomalies by changing the convergence of the momentum flux, thereby inducing positive feedback. Gong et al. (2010) found that in a zonally symmetric sense, anomalously strong anticyclonic RWB on the anticyclonic side of the jet leads to the positive SAM index (SAMI), whereas anomalously weak anticyclonic RWB in that area results in the negative SAMI. The previous studies of wave breaking in the SH have typically focused on the influence of RWB on the zonally averaged flow. By assuming an approximately zonally symmetric jet structure, these studies have not examined the spatial distribution of RWB, which is zonally asymmetric. Even though the jet structure in the SH is more zonally extended than in the NH, it is by no means zonally symmetric. Just as SM08 found that the NAMI was strongly forced in isolated regions, the SAMI may also be largely determined by wave breaking in isolated regions.

Observations indicate that the austral summer [December–February (DJF; summer)] SAMI over the past three decades has a positive linear trend (Marshall 2003; Fogt et al. 2009). Studies have attributed the positive trend in the SAMI to stratospheric ozone depletion and/or global warming (e.g., Thompson and Solomon 2002;

Arblaster and Meehl 2006; Kushner et al. 2001).² The dynamical characteristics that connect the SAM to these two external forcings are similar, and it has been hypothesized that they are associated with eddy–mean flow interaction. When the atmosphere responds to tropospheric warming and stratospheric cooling, the meridional temperature gradient across the midlatitude tropopause increases, which leads to an accelerated westerly jet. It has been hypothesized that the stronger westerly flow leads to an increase in eddy phase speed, inducing a more poleward eddy momentum flux convergence; this results in a poleward shift of the jet and a positive SAMI (Chen and Held 2007; Chen et al. 2008). Chen and Held (2007) also argue that the subtropical wave-breaking region shifts poleward.

A negative relationship between the SAM and El Niño–Southern Oscillation (ENSO) phases (Carvalho et al. 2005) is also believed to be related to eddy–mean flow interaction. A number of studies suggest that ENSO-induced positive sea surface temperature (SST) anomalies in the central Pacific strengthen the subtropical jet (e.g., Shapiro et al. 2001; Seager et al. 2005), affecting the convergence of eddy momentum flux (Lu et al. 2008), thereby changing the latitudinal migration of the jet (L’Heureux and Thompson 2006; Chen et al. 2008). Gong et al. (2010) inferred that the change in a measure of strength of anticyclonic RWB provides a connection between ENSO and the SAM.

In this study, we aim to answer the following questions:

- (i) What is the spatial distribution of anticyclonic and cyclonic RWB occurrence in the SH in summer?
- (ii) Are there isolated regions where anticyclonic and cyclonic RWB most effectively influence the SAMI?
- (iii) Do anticyclonic and cyclonic RWB frequencies exhibit a linear trend similar to the SAMI trend?
- (iv) How does anticyclonic and cyclonic RWB frequency change during different phases of ENSO in terms of its spatial–temporal characteristics?

Additionally, we want to verify that the seasonal-mean effect of RWB frequency on the SAMI translates to the short synoptic time scale of nontrivial sign changes in the SAMI over the order of 10 days. We adopt the methodology of diagnosing anticyclonic and cyclonic RWB in the NH from SM08 and adapt it to the SH to provide a hemispheric view of both types of RWB frequency. Correlation, composite, and time series analysis are performed to answer our questions. The paper is organized in the following way. Section 2 describes the data and methods.

¹ A paper by Ndarana and Waugh (2011) addressing SH RWB came to our attention at the proof stage.

² A paper by Polvani et al. (2011) that came to our attention at the proof stage presents convincing evidence that the trend in SAMI is due to stratospheric ozone depletion.

A climatology of seasonal-mean RWB frequency is provided in section 3. Composites of atmospheric fields corresponding to anticyclonic and cyclonic RWB are shown in section 4 and further insight into the regions where RWB and the SAM have a close relationship on an interannual time scale is explored in section 5. Section 6 describes how RWB helps explain interannual and intraseasonal SAM variability. The response of anticyclonic and cyclonic RWB to ENSO-induced SST anomalies is addressed in section 7. We then conclude with a discussion of our results in section 8.

2. Data and methodology

a. Data and indices

We use 6-hourly National Centers for Environmental Prediction–National Center for Atmospheric Research (NCEP–NCAR) reanalysis data that are of 2.5° latitude \times 2.5° longitude spatial resolution. Since reanalysis data in the SH were not of good quality before the satellite era because of sparse observations (Marshall 2003), we restrict the analysis to austral summers from December 1979 to February 2009 (30 summers). The SAM is computed using empirical orthogonal function (EOF) analysis on monthly 700-mb geopotential height anomalies south of 20°S for the period 1979–2000 (this is the method used by the Climate Prediction Center; see www.cpc.noaa.gov/products/precip/CWlink/daily_ao_index/history/method.shtml). The anomalies for each month are obtained by subtracting the time mean of the monthly 700-mb geopotential height of all years. The SAM is the leading EOF and its polarity is referred to as the SAMI. The monthly SAMI is constructed by projecting the monthly 700-mb geopotential height anomalies onto the leading EOF. The SAMI is normalized by the standard deviation of the principal component from the base period (1979–2000). Seasonal SAMI time series are calculated by time averaging three months (DJF) in each year. The 6-hourly SAMI is produced similarly, except by projecting 6-hourly geopotential height anomalies onto the leading EOF calculated from monthly data.

To analyze the relationship between RWB and ENSO, the average of the oceanic Niño index (ONI) in DJF each year is used (see www.cpc.noaa.gov/products/analysis_monitoring/ensostuff/ensoyears.shtml). A positive ONI represents the warm episode of SST and a negative ONI represents the cold episode in the Niño-3.4 region (5°N – 5°S , 120° – 170°W).

b. Methodology of RWB detection

We visualize RWB as irreversibly overturning PV contours on an isentropic surface (McIntyre and Palmer

1983). The methodology for detecting RWB is the same as described in SM08, but the latitudinal configuration is reversed in the SH. SM08 found that analyzing PV on the 350-K isentropic surface provided a useful representation of upper-tropospheric anticyclonic and cyclonic breaking over the largest range of latitudes. Also, we find that RWB frequency on the 350-K isentropic surface is well correlated with variability in the SAMI. The methodology for detecting RWB is briefly described here. First, we identify the longest circumpolar PV contours that intersect with a north–south meridian more than once. We examine all PV contours between 0 and -20 PVU ($1 \text{ PVU} \equiv 10^{-6} \text{ m}^2 \text{ s}^{-1} \text{ K kg}^{-1}$) at an interval of -0.5 PVU at each 6-hourly analysis time. Our method detects RWB from 40 different PV values on one isentropic surface (350 K), which is better than some conventional methods that detect only one PV value on one level, and then we examine several different levels to get the vertical distribution. When the longest PV contour has been identified as overturning, points bounding a poleward-advecting PV tongue are ordered to progress eastward along the contour and the latitude of these points is recorded (for more details, see appendix and Fig. 1 in SM08). We distinguish anticyclonic and cyclonic wave-breaking events by comparing the latitude of the first and last points arranged eastward. Referring to an anticyclonic RWB example in Fig. 1a, the first point (the southward intersection) encountering a breaking region is located more poleward than the last point (the northward intersection). For a cyclonic RWB example, the first point (the northward intersection) is located more equatorward than the last point (the southward intersection) (see Fig. 1b). In the SH, anticyclonic RWB events are deformed PV contours that are oriented southeast–northwest and cyclonic RWB events are oriented southwest–northeast. These orientations are opposite of their counterparts in the NH (SM08). Then we measure the zonal extent, the area of the PV tongue, and the location of the PV tongue’s centroid (open circle for anticyclonic and filled circle for cyclonic RWB in Fig. 1) in the latitude–longitude plane. The zonal extent of one breaking event is the span (along a great circle route in units of arc length) between the east and west boundaries of the PV tongue. To exclude meridionally elongated small-scale tongues, which are not counted as wave-breaking events, the zonal extent and the area of the tongue must satisfy a minimum size requirement (see appendix of SM08). To prevent counting a redundant centroid from the same breaking event, any centroids within limited distance (i.e., 5°) to the one from the largest tongue are removed. We divide the SH into 400 equal-area spatial bins and calculate the relative frequencies of anticyclonic and cyclonic RWB centroids within each bin as follows:

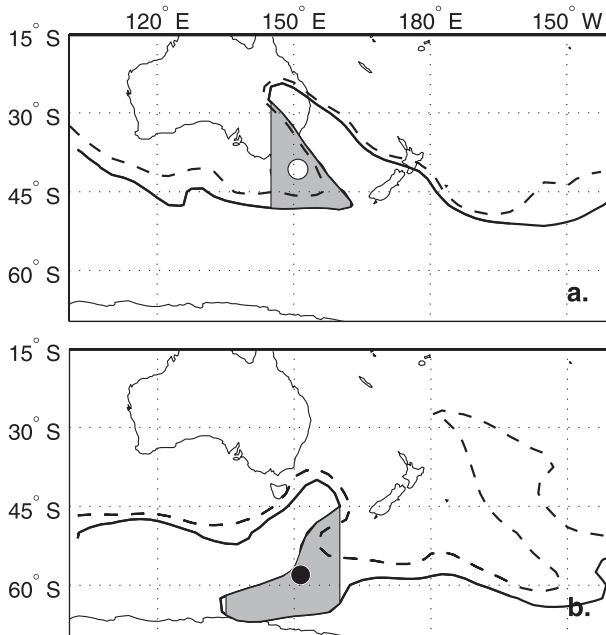


FIG. 1. (a) Anticyclonic RWB case on 8 Feb 1985 at 1800 UTC. Two PV contours are depicted: dashed contour is -3 PVU and solid contour is -4 PVU. (b) Cyclonic RWB case on 3 Jan 1983 at 1800 UTC. Dashed contour is -5 PVU, and solid contour is -6 PVU. Shading indicates areas of reversed PV gradients. Circles show locations of tongue centroids.

$$\gamma_a(h) \equiv \frac{1}{T} \sum_{t=1}^T \beta_a(h, t) \quad \text{and}$$

$$\gamma_c(h) \equiv \frac{1}{T} \sum_{t=1}^T \beta_c(h, t),$$

respectively. The integer $1 \leq h \leq 400$ represents each of the spatial bins; t is the time of a 6-hourly observation; T is the total number of 6-hourly observations during the period; β_a is 1 when there is an anticyclonic RWB centroid in bin h , otherwise it is 0; and β_c is defined likewise for cyclonic RWB events. The above frequencies indicate how often each type of RWB occurs at a specified location. As will be shown in section 3, the wave-breaking regions for both types of RWB overlap with areas of large zonal extent of breaking (Figs. 2a,b). Therefore, high RWB frequency also indicates that the wave breaking extends over a large area.

3. Climatology of anticyclonic and cyclonic RWB in summer

The SH summer (DJF) zonally averaged flow in the latitude–height plane is characterized by a single well-developed midlatitude jet (not shown). The subtropical jet is largely absent in summer because of the relatively

small heating difference between the tropics and subtropics (Lorenz and Hartmann 2001). However, the Antarctic continent provides a heat sink throughout the year and maintains a vigorous midlatitude baroclinic zone in summer (Trenberth 1991). The SH winter is characterized by a double jet structure (not shown) and the jets frequently have a wave-3 appearance, whereas the DJF jet is more zonally symmetric (e.g., Codron 2005). Since we want to examine the climatology of both anticyclonic and cyclonic RWB and their spatial relation to the mean jet, we limit this study to the SH summer, when spatial separation between breaking regions is clearer than in winter. The SH summer is also the season when a positive linear trend in the SAMI over the past 30 years has been observed.

a. The spatial pattern of RWB frequency

In Fig. 2a we present the relative frequency of anticyclonic RWB and in Fig. 2b the relative frequency of cyclonic wave breaking for DJF 1979–2009 (contours), along with the zonal extent of the breaks (shaded). The shading in Fig. 2c depicts the summer mean zonal wind on 350-K surface for the same period, so that the RWB frequency may be compared to theoretical ideas on Rossby wave propagation and anticyclonic/cyclonic RWB in shear flow. The contours in Fig. 2c show monthly anomalies in zonal wind regressed on the SAMI. Clearly, a poleward migration of the jet is associated with a positive SAMI, and an equatorward migration of the jet is associated with a negative SAMI.

Focusing on Fig. 2c, the SH summer jet at 350 K has a minimum downstream of New Zealand, resembling a split in the jet structure. The jet maximum is in a zonally elongated region south of South Africa. Compared to the clear regional structure of the NH jets, this is a single jet with some zonal variation in the time mean. The jagged equatorward shape of the time-mean jet in three locations suggests that these are areas of frequent large-scale anticyclonic breaking (e.g., Magnusdottir and Haynes 1999). These locations include the east Pacific close to the west coast of South America, at lower latitude in the central to east Atlantic, and in the Indian Ocean upstream of Australia. Indeed, Fig. 2a verifies that these are regions of frequent large-scale anticyclonic RWB. Additionally, an area of frequent anticyclonic RWB is at the downstream end of the jet in the New Zealand region, which is reminiscent of the preferred locations of anticyclonic RWB in the NH (SM08; Abatzoglou and Magnusdottir 2006), downstream of the two jets. The area of frequent anticyclonic RWB forms one zonally extensive region on the anticyclonic side of the jet with local maxima in the above-mentioned areas. This is different from anticyclonic RWB in the NH winter, where isolated maxima of RWB

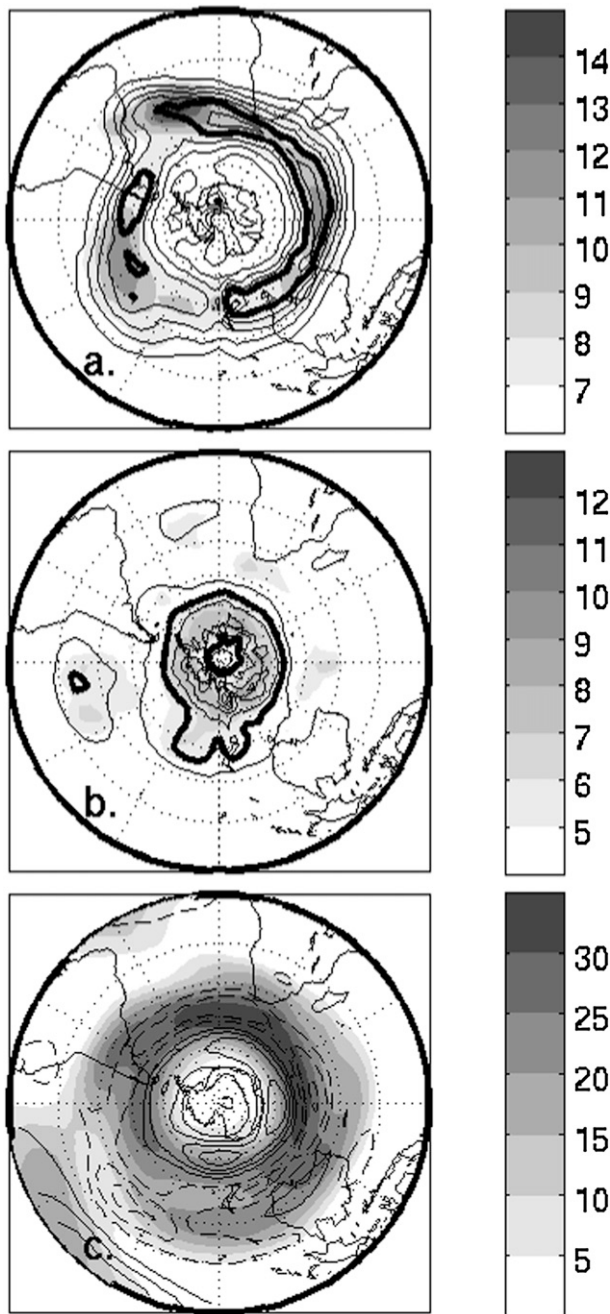


FIG. 2. (a) Shading shows mean zonal extent of breaks in units of arc length. Contours show relative frequency of anticyclonic RWB (γ_a) for DJF 1979–2009 with contour interval of 0.02. Bold contour marks 0.1. (b) As in (a), but for cyclonic RWB (γ_c) with bold contour marking 0.04. (c) Mean zonal wind speed on 350-K isentropic surface with shading at intervals of 5 m s^{-1} . Contours show monthly anomalies in zonal wind regressed on SAMI (solid contours for positive values and dashed contours for negative values every 1 m s^{-1} ; zero contour is omitted).

(associated with the two jets) are normal (SM08). It is worth noting the two patches of equatorward-extending (or equatorward trailing) regions of higher-frequency anticyclonic RWB. One patch is in the area upstream of the jet maximum in the western South Atlantic (60°W – 0°). The other patch is in the southeast to south-central Pacific (150° – 90°W). Both regions of maximum wave-breaking frequency (surf zones) correspond to the areas containing the spatially most extensive anticyclonic breaks.

The frequency of cyclonic RWB is shown in Fig. 2b. It is considerably less frequent than anticyclonic RWB and mostly confined to the high latitudes, poleward of 60°S , or to the cyclonic side of the jet. The exception is in the region of the split jet structure downstream of New Zealand, where the relative frequency of cyclonic RWB exceeds 0.04 at 45°S . (Note that the bold contour in Fig. 2a represents 0.1 and in Fig. 2b it represents 0.04.)

To summarize, our results show that anticyclonic RWB tends to take place in a zonally elongated belt on the equatorward (or anticyclonic) side of the jet, and cyclonic RWB tends to take place in a high-latitude area poleward of the jet maximum (or on the cyclonic side of the jet). Almost all the anticyclonic RWB cases take place in the 30° – 60°S latitude belt, whereas almost all the cyclonic RWB cases take place between 45° and 75°S . Note that the areas of maximum RWB are less zonally symmetric than the jet structure; however, they are considerably more zonally extensive than in the NH (SM08).

b. The SAM trend and RWB occurrence

Interestingly, the time series of anticyclonic RWB occurrence has a significant positive linear trend during the past three decades. The bold curve in Fig. 3a shows the total number of summer anticyclonic RWB occurrences each year within the 30° – 60°S latitude band as a function of year. For comparison, the thin curve shows the SAMI for the same period. The summer SAMI and the sum of anticyclonic summer RWB occurrences are highly correlated with a correlation coefficient of 0.83. When we fit a line to each curve in Fig. 3a, both slopes are positive and statistically significant.

A similar plot for cyclonic wave breaking (shown in bold in Fig. 3b) within the 45° – 75°S latitude belt, where almost all the cyclonic wave breaking is taking place, reveals a slightly negative linear trend as shown by the best-line fit (bold dashed–dotted line). The SAMI is also shown in Fig. 3b for comparison. The linear trend of the best-fit line is not significant. The SAMI and the sum of cyclonic RWB occurrences are not significantly correlated either. In the next section, we examine the effect of both types of RWB on the background flow field by examining a composite of both types of breaking. Then we go on to examine which areas of RWB are most

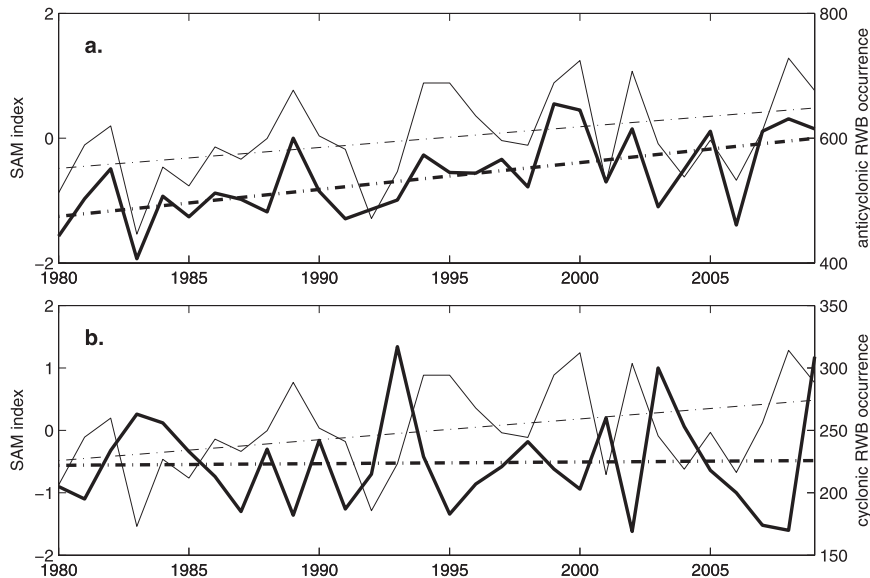


FIG. 3. Annual SH summer SAMI, shown by thin curve in both panels. (a) Bold curve is anticyclonic RWB occurrence in 30°–60°S band per austral summer 1979–2009. (b) Bold curve is cyclonic RWB occurrence in 45°–75°S band during same period. Dashed–dotted line shows best-fit line.

important in influencing the SAMI on interannual time scales.

4. Composite analysis of the kinematic effect of RWB

We have seen that summer RWB tends to be latitudinally localized, with anticyclonic RWB primarily taking place in the 30°–60°S latitude band (Fig. 2a) and cyclonic RWB primarily taking place in the 45°–75°S latitude band (Fig. 2b). Here we examine the effects of each type of breaking on the background flow field by way of a composite analysis.

We calculated deviations of 350-K horizontal wind and 700-mb geopotential height for each observation time from the time mean over all observation times for DJF of all years, 1979–2009. We computed the horizontal divergence of the \mathbf{E} vector ($\nabla \cdot \mathbf{E}$) (Hoskins et al. 1983). Under quasigeostrophic scaling, $\nabla \cdot \mathbf{E}$ appears in the time-mean zonal momentum equation as the forcing of the zonal flow by the transient eddies (see appendix A in Hoskins et al. 1983). Areas where $\nabla \cdot \mathbf{E}$ is positive correspond to the westerly acceleration of the zonal flow, whereas negative $\nabla \cdot \mathbf{E}$ corresponds to the westerly deceleration of the flow.

We composited fields of $\nabla \cdot \mathbf{E}$, horizontal wind, and geopotential height when anticyclonic and cyclonic RWB occurred. We collected 16 118 anticyclonic wave-breaking occurrences in the 30°–60°S zonal band, overlaid them so that the wave-breaking centroids were in the same location, and then averaged them over the composited fields on

the 350-K isentropic and the 700-mb isobaric surfaces, respectively. We collected 6718 cyclonic wave-breaking occurrences in the same fashion, in the primary latitudinal band of cyclonic wave breaking, 45°–75°S. In each case, we required that breaks included in the composite have similar size characteristics to ensure spatial alignment.

Figures 4a and 4b show $\nabla \cdot \mathbf{E}$ for anticyclonic and cyclonic RWB composites, respectively (contours), with the composite wind field superposed (arrows). The limited average in longitude (taken over -30° to 30° relative longitude, centered on the centroid) of $\nabla \cdot \mathbf{E}$ of the composite is shown to the right of each frame. Consistent with results in the NH (SM08), anticyclonic RWB results in the acceleration of the flow poleward and deceleration of the flow equatorward of the anticyclonic wave-breaking centroid, whereas cyclonic RWB results in the deceleration of the flow poleward and acceleration of the flow equatorward of the cyclonic centroid. Note that the composite field of $\nabla \cdot \mathbf{E}$ for both anticyclonic and cyclonic wave breaking is more zonally extended in the SH (Figs. 4a and 4b) compared to that in the NH (Figs. 3a and 3b in SM08). This may be due to the slightly different shapes of baroclinic eddies in the SH. When we look at the projection on the SAM by examining geopotential height on the 700-mb pressure surface in each of the anticyclonic and cyclonic composites (Fig. 4c for anticyclonic and Fig. 4d for cyclonic RWB), there is clear correspondence to the effect of RWB on the NAM in the NH. In particular, the anticyclonic RWB composite is associated with negative (positive) height anomalies poleward (equatorward) of the composite

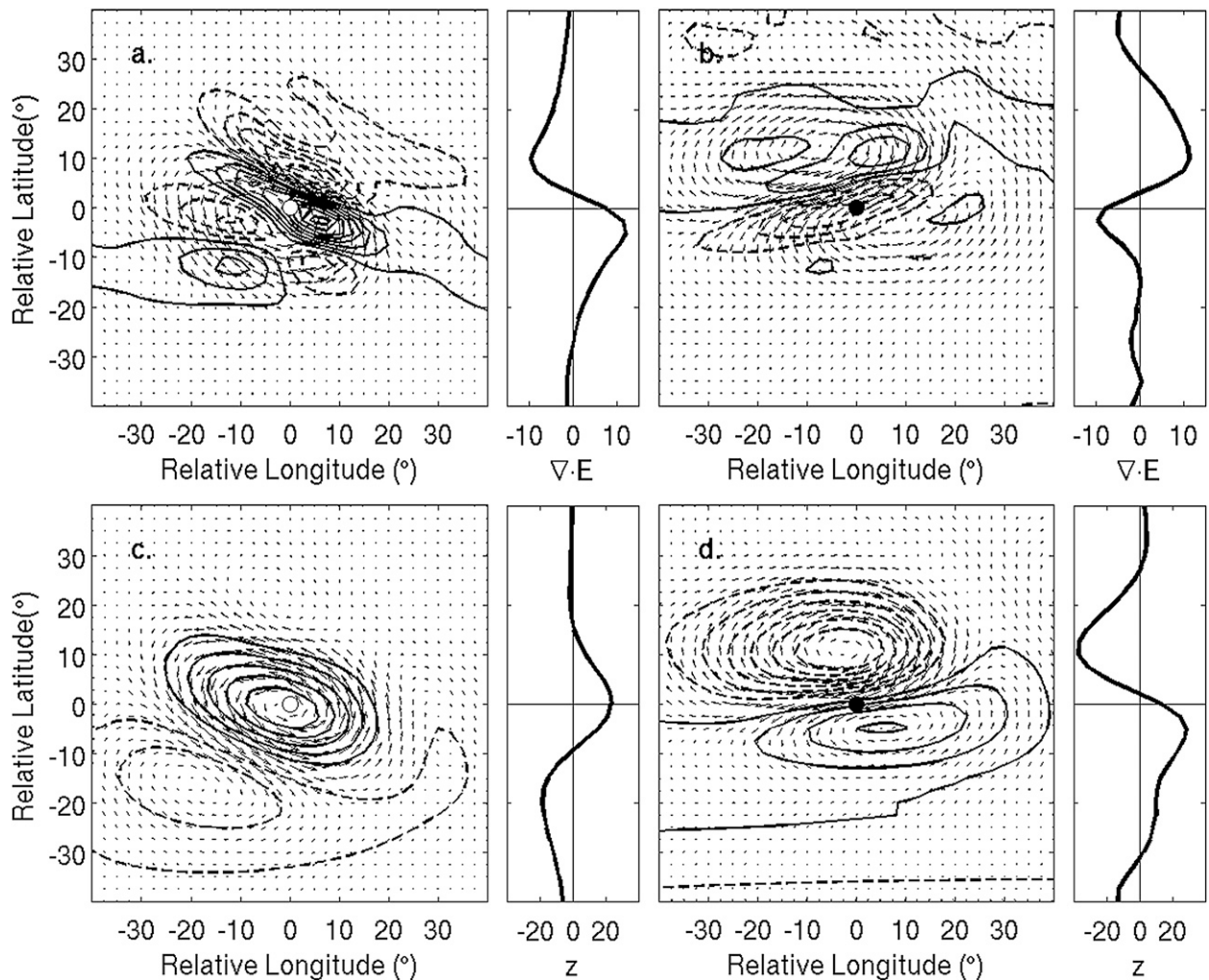


FIG. 4. (a) The $\nabla \cdot \mathbf{E}$ (contours) and wind vectors (arrows) on 350 K after averaging composite cases for anticyclonic RWB. Solid (dashed) contours show positive (negative) $\nabla \cdot \mathbf{E}$ with $1 \times 10^{-4} \text{ m s}^{-2}$ contour interval. (b) As in (a), but for cyclonic RWB. Panels to right of (a) and (b) show composite longitudinal average of $\nabla \cdot \mathbf{E}$ ($1 \times 10^{-5} \text{ m s}^{-2}$) from -30° to 30° relative longitude, centered on breaking centroid. (c) Geopotential height anomalies on 700 mb contoured at 10-m intervals and wind vectors on 700 mb (arrows) after averaging over all anticyclonic RWB composite cases. (d) As in (c), but for cyclonic RWB. Panels to right of (c) and (d) show composite longitudinal average over -30° to 30° relative longitude of geopotential height anomalies (m). Zero contour is omitted in all plots.

centroid (Fig. 4c). This corresponds to a positive SAMI for a centroid located close to the center of the 30° – 60° S latitude band. The cyclonic RWB composite (Fig. 4d) is associated with positive (negative) height anomalies poleward (equatorward) of the composite centroid. In this case the composite is drawn from the 45° – 75° S latitude band. According to Fig. 4d, cases that are collected from the more equatorward part of the domain would certainly be expected to project onto the negative polarity of the SAM. The effect of RWB on the resulting signature in the annular mode depends on the latitude of the jet relative to the location of RWB.

The analysis in this section focused on one side of the wave–mean flow interaction or how RWB obtained by

composite analysis may affect the background zonal flow field. The previous section (section 3) analyzed where RWB is occurring in relation to the time-mean jet. However, the seasonal-mean jet may be subject to a slight shift to higher latitudes through time by external forcing. In the next section, we examine how RWB affects the SAM locally instead of focusing on composite analysis from zonal bands.

5. Local regions where RWB affects the SAM

According to Fig. 3, the summer SAMI is closely correlated with the number of anticyclonic RWB occurrences in the SH. In this section, we take a closer look at the

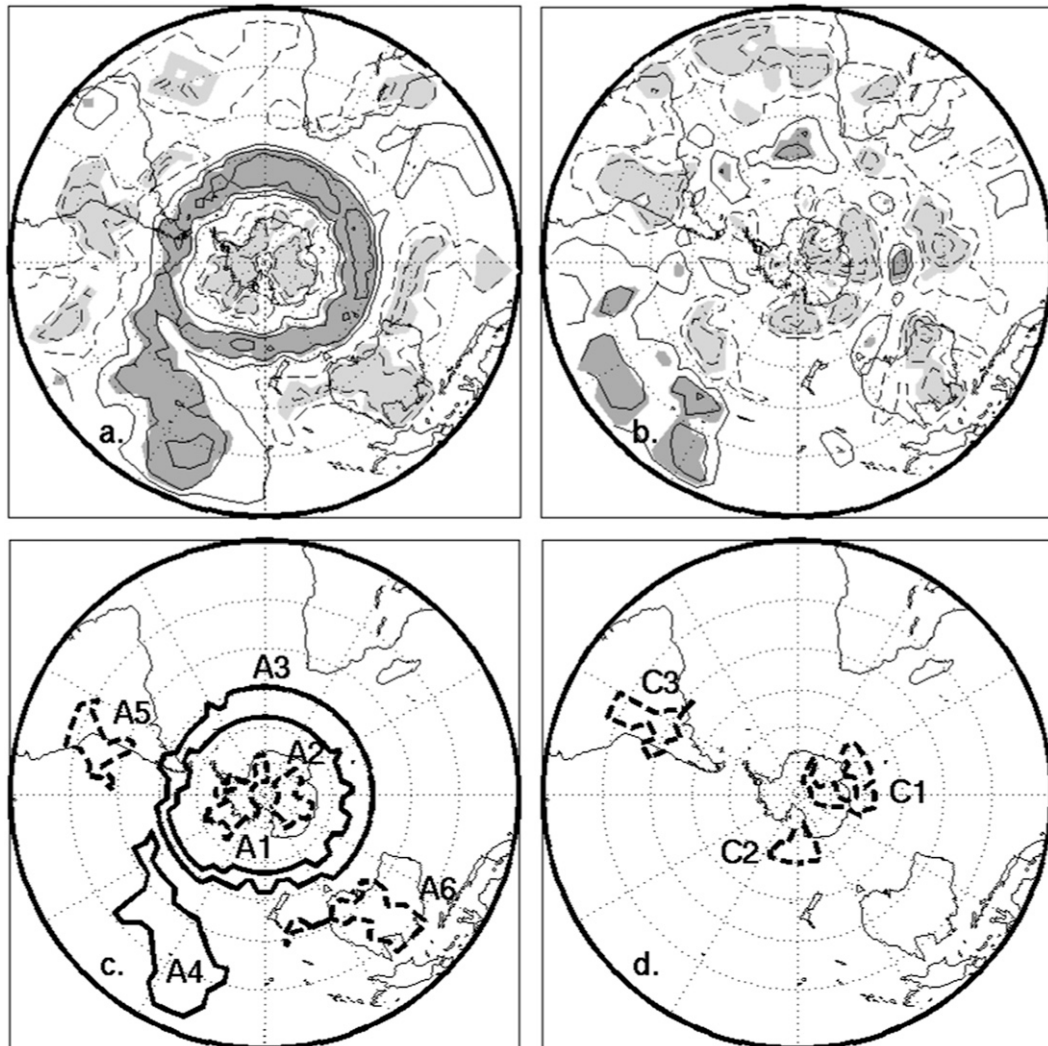


FIG. 5. (a) Correlation coefficients of relative frequency of anticyclonic RWB (γ_a) summed over each austral summer vs SAMI averaged over each summer are contoured by 0.2. Zero contour is omitted. Solid (dashed) contours indicate positive (negative) values. Regions where positive (negative) correlation is significant at 95% confidence level (using the t test) are dark (light) shaded. (b) As in (a), but for relative frequency of cyclonic RWB (γ_c) vs SAMI. (c) Regions where γ_a is significantly correlated with SAMI. Solid contours show regions that are positively correlated with SAMI; dashed contours show regions that are negatively correlated. (d) As in (c), but for γ_c .

locations where RWB affects the SAMI the most. The correlation between the SAMI averaged over each summer and the RWB relative frequency that has been calculated at each point and summed over the summer is shown in Figs. 5a and 5b, where shading indicates significance at the 95% confidence level according to the t test. Figure 5a shows the correlation between anticyclonic RWB frequency (γ_a) and the SAMI. Figure 5b shows the correlation between cyclonic RWB frequency (γ_c) and the SAMI. Regions where RWB affects the SAM significantly are defined as the shaded bounded areas in Fig. 5a and 5b, but we ignore the shaded area involving cyclonic RWB in

the tropical central Pacific because of the very few cyclonic RWB instances at this location. We also ignore shaded areas that are smaller than 20° latitude \times 20° longitude. Regions A1–A6 (shown in Fig. 5c) refer to areas where the time series of anticyclonic RWB and SAMI are significantly correlated. Regions C1–C3 (shown in Fig. 5d) refer to areas where the time series of cyclonic RWB and SAMI are significantly correlated.

Region A3 is the most noticeable positively correlated region. It is zonally extended, centered at 50° S. It is wider in latitude in the Indian and Atlantic sectors than in the Pacific sector. The shape and the location of this

zonally extended region are similar to that of maximum γ_a in the midlatitudes shown in Fig. 2a. This significantly correlated latitudinal zone differs from the strongly correlated regions in the NH, which are quite localized (SM08, see their Fig. 5). Since the SAM is characterized by a stronger annular structure than the NAM, this difference seems to coincide with the different morphology of the annular mode in the respective hemisphere. Poleward of region A3 are the negatively correlated cyclonic RWB regions C1 and C2 in the eastern hemisphere. Equatorward of region A3 are the negatively correlated anticyclonic RWB regions, region A5 in the east Pacific sector, and region A6 over Australia. One positively correlated region, A4, stretches farther equatorward than any other region or into the subtropical central Pacific, overlapping with the area of strong SST anomalies during ENSO and overlapping with the location of the South Pacific convergence zone. Regions with significant correlation between cyclonic RWB and the SAMI are shown in Fig. 5d. They are both smaller in area and fewer in number compared to the counterparts associated with anticyclonic RWB. All are negatively correlated with the SAMI.

The composite analysis can help explain the relationship between RWB and the SAMI in some correlated regions. Since the A3 region is within the 30°–60°S latitudinal band where anticyclonic RWB tends to generate the positive SAM signature, it suggests a positive correlation between γ_a and the SAMI in this region. We shall return to considering the A4 region in section 7.

6. Time series analysis

a. Interannual analysis of RWB and the SAM

We examine which of the objectively defined RWB regions are needed to account for the variability of the SAMI on a year-to-year basis by building a multivariate linear regression model. In the regression model, the candidate predictors are a set of wave-breaking indices, which are defined as the sum of RWB relative frequency for each austral summer within the objectively defined regions. For example, A1 refers to the time series of $\Sigma\gamma_a$ from region A1, and C1 refers to the time series of $\Sigma\gamma_c$ from region C1.

The first step in building a multivariate linear regression model is to find which predictors are significant to the SAMI by bootstrapping, using stepwise backward regression. When predictors appear in more than 60% of the bootstrap samples, these predictors can yield an effectively predictive model (Austin and Tu 2004). To apply this method, we produced a new sample of index time series by bootstrapping with replacements and calculating the predictors included in the stepwise backward

regression model. After repeating this bootstrap predictor selection procedure 1000 times, two predictors—A3 and C1—appeared more than 600 times, and thus they are determined to affect the SAMI significantly. We built a two-predictor multivariate regression model using least squares since the value of the information criterion from Akaike (1974) is small.

The least squares scheme yields the following two-predictor model to simulate the SAMI in each austral summer:

$$\text{SAMI} = 0.75(\text{A3}) - 0.22(\text{C1}).$$

The intercept is almost 0. The model accounts for 81% of the annual SAMI variability and suggests that A3 plays the dominant role in the variability of the SAMI. In fact, 78% of the SAMI can be captured by a single-variable model using A3 only. The result is reasonable because region A3 is the largest defined region in the latitudinal band between 40° and 50°S, extending around much of the hemisphere. The effect of cyclonic RWB in region C1 is confined to the high latitudes in the Indian Ocean. In section 3b we found that the trend in SAMI resembles the trend in anticyclonic RWB frequency in the 30°–60°S latitude band. Since the A3 region is located inside this latitude band and A3 also shows the significant positive trend (not shown), the trend in SAMI is associated with the trend of A3.

In light of the significant trend of the SAMI, it is of interest to ask whether wave-breaking indices capture the variability of the SAMI without the linear trend. To answer this question, we detrended the SAMI and the wave-breaking indices. After removing the trend, the polarity of the SAMI time series changes little. The new model from detrended data differs only slightly from that with raw data, that is,

$$\text{SAMI}_{\text{detrended}} = 0.82(\text{A3}_{\text{detrended}}) - 0.28(\text{C1}_{\text{detrended}}).$$

The indices A3 and C1 keep their place as the most important predictors in the regression model and capture the SAMI variability (not shown). Inclusion of the interaction between indices does not change the predictability of these two models noticeably, so it is neglected (not shown). To summarize, both multivariate linear regression models with raw and detrended data are promising when predicting the time series of the raw and detrended SAMI in terms of corresponding wave-breaking indices.

b. Within-season analysis of RWB and the SAM

The multivariate linear regression model addresses the relation of the SAMI to A3 and C1 on a seasonal-mean

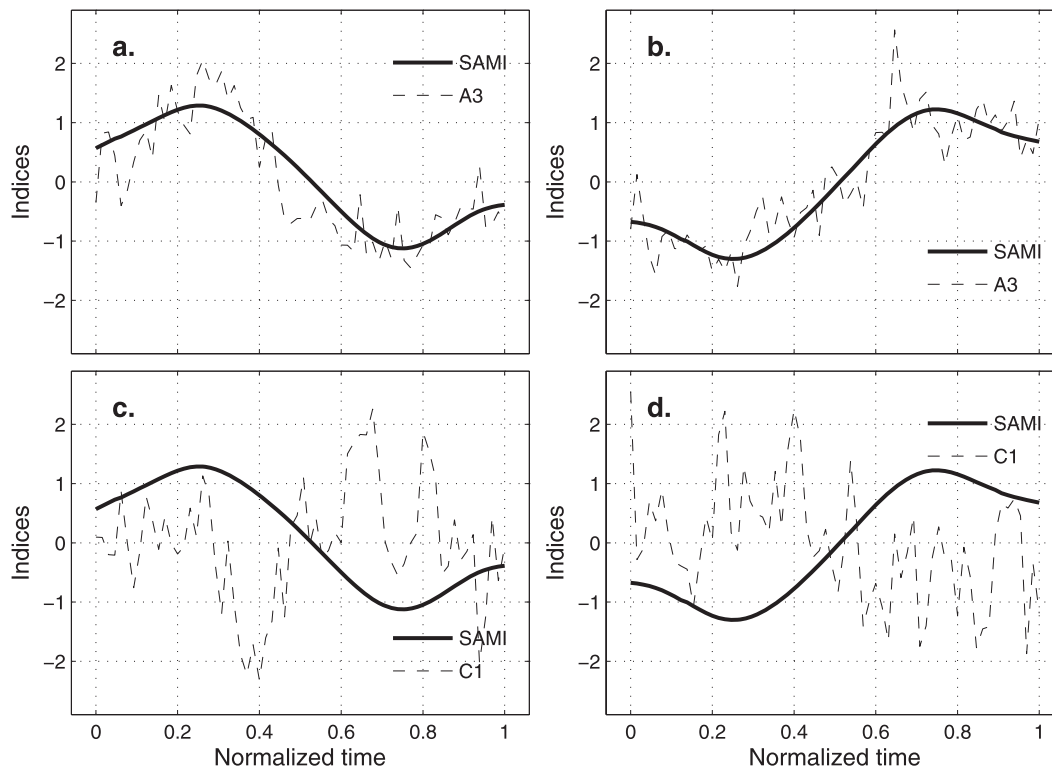


FIG. 6. (a) Composite of A3 (thin dashed line) with negative transitional class of normalized 10-day low-pass SAMI (thick solid line). Threshold value is 0.4. (b) As in (a), but for positive transitional class of normalized 10-day low-pass SAMI. (c) As in (a), but for composite of C1 (thin dashed line). (d) As in (c), but for positive transitional class of normalized 10-day low-pass SAMI.

basis. It is interesting to investigate this relation on the within-season time scale. The time lag between indices is also examined to clarify the connection between wave-breaking events and the jet displacement.

To implement within-season analysis, we proceed as in Kidson and Watterson (1999) and use a 10-day low-pass filter to smooth the time series of 6-hourly SAMI. The smoothed SAMI successfully captures the behavior of the unsmoothed SAMI (not shown). The smoothing helps to detect transitions in the SAMI, but it does not prevent the detection of RWB events during these transitions. We composite the time series of RWB indices as the smoothed SAMI reverses its sign. Two classes of transitions are identified: (i) an “N class” transition is defined when the smoothed SAMI changes from a positive maximum to a negative minimum and (ii) a “P class” transition is defined when the SAMI changes from a negative minimum to a positive maximum. The threshold for maxima and minima for both positive and negative transitions is chosen as 0.4. The relation between the transitions of the SAMI and RWB indices is not sensitive to the threshold value, in that it does not change Fig. 6; although, the larger a threshold, the fewer the transition cases. Adopting this threshold, there are 26 cases for the

N-class transition and 26 cases for the P-class transition in the 30-yr record. The duration for N-class cases from a local maximum to a local minimum ranges from 7 to 23 days with an average of 12.07 days. The duration for P-class cases from a local minimum to a local maximum ranges from 6 to 20 days with an average of 12.09 days. We normalize the time extent by extending backward and forward half of the time frame for each transition. The new time axis is normalized so that it extends from zero to one. The local maximum was set at 0.25 and the local minimum was set at 0.75 for the N-class transitions (Figs. 6a and 6c). For the P-class transitions, the local minimum was set at 0.25 and the local maximum was set at 0.75 (Figs. 6b and 6d).

Figures 6a and 6b show that on this short time scale, A3 closely resembles the variability of the smoothed SAMI in both the negative and positive transitions. The composite of A3 is correlated with the N-class transition of the SAMI with a correlation coefficient of 0.88. It is correlated with the P-class transition of the SAMI with a coefficient of 0.90. The time series of C1 is negatively correlated with the SAMI, which is particularly apparent in the P-class transition (Fig. 6d). The correlation coefficient between C1 composites and the P-class transition

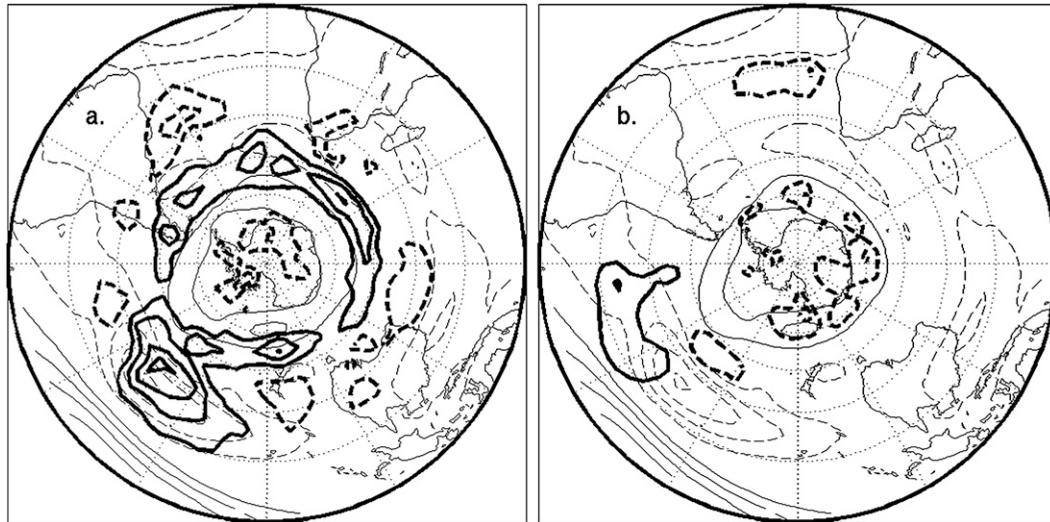


FIG. 7. Thick contours represent difference of RWB frequency ($\Delta\gamma_a$ for anticyclonic and $\Delta\gamma_c$ for cyclonic) between four chosen La Niña years and four chosen El Niño years on 350 K for DJF. Thin contours show difference of mean zonal wind ($\Delta\bar{u}$) on 350 K calculated from same period. (a) For anticyclonic RWB. (b) For cyclonic RWB. Thick contour interval is 0.02, and 0 contour is suppressed. Thin contour interval is 5 m s^{-1} , and 0 contour is also suppressed. In all cases, solid contours are positive and dashed contours are negative.

of the SAMI is -0.51 , more negative than that between C1 and the N-class transition of the SAMI, which is -0.32 . There is no time lag between the transition of the smoothed SAMI and RWB indices A3 and C1. The result suggests that the SAMI responds to anticyclonic RWB in the A3 region and cyclonic RWB in the C1 region contemporaneously. The result also implies that even though cyclonic RWB generates a clear negative SAM signature (Fig. 4d), the more localized nature of the C1 region limits its kinematic effect on the transition of the SAMI.

7. RWB during ENSO cycles

In the years between 1979 and 2009, four strong El Niño years and four strong La Niña years have occurred. All of them have $|\text{ONI}| \geq 1.2$ for the austral summer. The seasons of 1982/83, 1991/92, 1997/98, and 2002/03 represent El Niño years with $\text{ONI} \geq 1.2$. The seasons of 1988/89, 1998/1999, 1999/2000, and 2007/08 represent La Niña years, all with $\text{ONI} \leq -1.4$.

The four strong El Niño summers were quite similar in terms of the upper-tropospheric zonal wind field and very different from the four strong La Niña summers, which were quite similar among themselves. We averaged the zonal wind on the 350-K isentropic surface over the La Niña seasons and over the El Niño seasons and computed the difference. The thin contoured field in Figs. 7a and 7b represents $\Delta\bar{u} = \bar{u}(\text{La Niña}) - \bar{u}(\text{El Niño})$. Similarly, we computed the difference in

RWB frequency for both anticyclonic ($\Delta\gamma_a$, shown in Fig. 7a) and cyclonic ($\Delta\gamma_c$, shown in Fig. 7b) wave breaking by subtracting the mean RWB frequency during the four El Niño summers from the four La Niña summers (depicted by thick contours).

The largest amplitude signature in $\Delta\bar{u}$ is in the equatorial Pacific, corresponding to increased westerlies of up to 20 m s^{-1} during La Niña compared to during El Niño. There is an opposite and smaller amplitude signature in $\Delta\bar{u}$ in the equatorial Atlantic. The most noticeable extratropical signature in $\Delta\bar{u}$ is a poleward shift in the jet. The signature of this poleward shift in the jet is seen in the $\Delta\gamma_a$ field in Fig. 7a, with a pronounced increase in anticyclonic RWB poleward of the maximum RWB region in the climatological γ_a field (shown in Fig. 2a) and a slight decrease in $\Delta\gamma_a$ in the region of maximum γ_a in climatology (Fig. 2a). The extratropical area of positive $\Delta\gamma_a$ overlaps the A3 region (defined in section 5), where anticyclonic RWB is highly correlated with the positive SAMI. The kinematic effects of RWB that were discussed in section 4 also support the notion that La Niña (El Niño) events are associated with positive SAMI (negative SAMI), and it is in agreement with previous work on the zonally averaged response (Gong et al. 2010 and references therein). Figure 7b shows that the difference in cyclonic RWB between the two ENSO extremes is only modest.

There is a zonally asymmetric signature in the $\Delta\gamma_a$ field in the central Pacific that has a strong subtropical component. The zonal flow in the subtropical Pacific is up to

20 m s^{-1} decreased during La Niña compared to El Niño years. The weak zonal flow results in a substantial increase in γ_a during La Niña years compared to El Niño years, in a region that overlaps the A4 region (defined in section 5), where RWB is strongly correlated with the positive SAMI. To examine this zonal asymmetry further, we calculated the field of $\Delta\gamma_a$ as a function of latitude integrated in longitude over 120° – 180°W (or the central Pacific) and compared it to $\Delta\gamma_a$ integrated over all other longitudes as a function of latitude (not shown). The annular-type signature outside the central Pacific is quite prominent with a positive maximum at 50°S and negative minimum at 30°S , corresponding to the jet shift and the associated shift in anticyclonic RWB in regions A3, A5, and A6. The central Pacific signature has positive values or increased $\Delta\gamma_a$ at all latitudes, with one maximum at about 30°S . This signature in the central Pacific is due to increased RWB during La Niña compared to El Niño in the region A4, which is correlated with the positive SAMI. However, one cannot deduce from this analysis that this correlation is due to anticyclonic RWB or wave–mean flow interactions in the A4 region by itself, since the different anticyclonic RWB regions (A3–A6) are highly correlated.

8. Concluding remarks

We have presented a Southern Hemispheric view of the spatial distribution of anticyclonic and cyclonic RWB in austral summer, adapting the method of RWB detection introduced in SM08 to the SH. Differences and similarities between the Southern and Northern Hemispheres in terms of RWB characteristics and the relationship with the annular modes were also addressed.

Our results show that the frequency of anticyclonic RWB is highest in a zonally extended region that has a maximum in the Eastern Hemisphere centered at 45°S or on the anticyclonic side of the mean jet (located at 50°S). The highest frequency of cyclonic RWB is anchored around the margins of the Antarctic continent, somewhat removed from the jet location. As a result, cyclonic RWB contributes considerably less to southern annular variability than anticyclonic RWB. In fact, 78% of the variability of the summer-mean SAMI can be explained by the summer-mean frequency of anticyclonic RWB in the aforementioned region (called region A3). Moreover, there is close correspondence between the positive trend in summer-mean SAMI over the 30 yr and the trend in anticyclonic RWB frequency in region A3. Note that this does not imply a causal relationship. As discussed earlier, the trend in the SAMI has been associated with a poleward migration and strengthening of the mean jet because of the increased slope through

time of the extratropical tropopause that has been linked to ozone depletion as well as anthropogenic warming (cooling) of the troposphere (stratosphere). We find that on the synoptic time scale (on the order of 10 days), nontrivial sign change in the SAMI from positive to negative (from negative to positive) values is associated with an increase (decrease) of anticyclonic RWB frequency in region A3. The association between SAMI and anticyclonic RWB is thus robust on different time scales.

We indicate how anticyclonic and cyclonic RWB frequency responds to the varying background flow during ENSO by examining four strong ENSO seasons of each sign and examining the mean difference in zonal flow and RWB frequency between them (La Niña minus El Niño). We find an increase in RWB in the region of the tropical/subtropical central Pacific that is related to the strong local decrease in zonal wind during La Niña compared to El Niño. At the same time, anticyclonic RWB at subtropical latitudes outside the central Pacific decreases and anticyclonic RWB at higher latitudes increases—all of which contribute to a positive SAMI.

Acknowledgments. We thank Joss Matthewman and Court Strong for their helpful discussions and three anonymous reviewers for their comments on the manuscript. This work was supported by NOAA Grants NA06OAR4310149 and NA09OAR4310132.

REFERENCES

- Abatzoglou, J. T., and G. Magnusdottir, 2006: Planetary wave breaking and nonlinear reflection: Seasonal cycle and interannual variability. *J. Climate*, **19**, 6139–6152.
- Akaike, H., 1974: A new look at the statistical model identification. *IEEE Trans. Autom. Control*, **AC19**, 716–723.
- Arblaster, J. M., and G. A. Meehl, 2006: Contributions of external forcings to southern annular mode trends. *J. Climate*, **19**, 2896–2905.
- Austin, P. C., and J. V. Tu, 2004: Bootstrap methods for developing predictive models. *Amer. Stat.*, **58**, 131–137.
- Benedict, J. J., S. Lee, and S. B. Feldstein, 2004: Synoptic view of the North Atlantic Oscillation. *J. Atmos. Sci.*, **61**, 121–144.
- Berrisford, P., B. J. Hoskins, and E. Tyrlis, 2007: Blocking and Rossby wave breaking on the dynamical tropopause in the Southern Hemisphere. *J. Atmos. Sci.*, **64**, 2881–2898.
- Carvalho, L. M. V., C. Jones, and T. Ambrizzi, 2005: Opposite phases of the Antarctic Oscillation and relationships with intraseasonal to interannual activity in the tropics during the austral summer. *J. Climate*, **18**, 702–718.
- Chen, G., and I. M. Held, 2007: Phase speed spectra and the recent poleward shift of Southern Hemisphere surface westerlies. *Geophys. Res. Lett.*, **34**, L21805, doi:10.1029/2007GL031200.
- , J. Lu, and D. M. W. Frierson, 2008: Phase speed spectra and the latitude of surface westerlies: Interannual variability and global warming trend. *J. Climate*, **21**, 5942–5959.
- Codron, F., 2005: Relation between annular modes and the mean state: Southern Hemisphere summer. *J. Climate*, **18**, 320–330.

- Feldstein, S. B., 2000: The timescale, power spectra, and climate noise properties of teleconnection patterns. *J. Climate*, **13**, 4430–4440.
- Fogt, R. L., J. Perlwitz, A. J. Monaghan, D. H. Bromwich, J. M. Jones, and G. J. Marshall, 2009: Historical SAM variability. Part II: Twentieth-century variability and trends from reconstructions, observations, and the IPCC AR4 models. *J. Climate*, **22**, 5346–5365.
- Gong, T. T., S. B. Feldstein, and D. H. Luo, 2010: The impact of ENSO on wave breaking and southern annular mode events. *J. Atmos. Sci.*, **67**, 2854–2870.
- Hitchman, M. H., and A. S. Huesmann, 2007: A seasonal climatology of Rossby wave breaking in the 320–2000-K layer. *J. Atmos. Sci.*, **64**, 1922–1940.
- Hoskins, B. J., I. N. James, and G. H. White, 1983: The shape, propagation and mean-flow interaction of large-scale weather systems. *J. Atmos. Sci.*, **40**, 1595–1612.
- Kidson, J. W., and I. G. Watterson, 1999: The structure and predictability of the “high-latitude mode” in the CSIRO9 general circulation model. *J. Atmos. Sci.*, **56**, 3859–3873.
- Kushner, P. J., I. M. Held, and T. L. Delworth, 2001: Southern Hemisphere atmospheric circulation response to global warming. *J. Climate*, **14**, 2238–2249.
- L’Heureux, M. L., and D. W. J. Thompson, 2006: Observed relationships between the El Niño–Southern Oscillation and the extratropical zonal-mean circulation. *J. Climate*, **19**, 276–287.
- Lorenz, D. J., and D. L. Hartmann, 2001: Eddy–zonal flow feedback in the Southern Hemisphere. *J. Atmos. Sci.*, **58**, 3312–3327.
- Lu, J., G. Chen, and D. M. W. Frierson, 2008: Response of the zonal mean atmospheric circulation to El Niño versus global warming. *J. Climate*, **21**, 5835–5851.
- Magnusdottir, G., and P. H. Haynes, 1999: Reflection of planetary waves in three-dimensional tropospheric flows. *J. Atmos. Sci.*, **56**, 652–670.
- Marshall, G. J., 2003: Trends in the southern annular mode from observations and reanalyses. *J. Climate*, **16**, 4134–4143.
- Martius, O., C. Schwierz, and H. C. Davies, 2007: Breaking waves at the tropopause in the wintertime Northern Hemisphere: Climatological analyses of the orientation and the theoretical LC1/2 classification. *J. Atmos. Sci.*, **64**, 2576–2592.
- McIntyre, M. E., and T. N. Palmer, 1983: Breaking planetary waves in the stratosphere. *Nature*, **305**, 593–600.
- Nakamura, M., and R. A. Plumb, 1994: The effects of flow asymmetry on the direction of Rossby wave breaking. *J. Atmos. Sci.*, **51**, 2031–2045.
- Ndarana, T., and D. W. Waugh, 2011: A climatology of Rossby wave breaking on the Southern Hemisphere tropopause. *J. Atmos. Sci.*, **64**, 798–811.
- Polvani, L. M., D. W. Waugh, G. J. P. Correa, and S.-W. Son, 2011: Stratospheric ozone depletion: The main driver of twentieth-century atmospheric circulation changes in the Southern Hemisphere. *J. Climate*, **24**, 795–812.
- Rivière, G., and I. Orlanski, 2007: Characteristics of the Atlantic storm-track eddy activity and its relation with the North Atlantic Oscillation. *J. Atmos. Sci.*, **64**, 241–266.
- Seager, R., N. Harnik, W. A. Robinson, Y. Kushnir, M. Ting, H. P. Huang, and J. Velez, 2005: Mechanisms of ENSO-forcing of hemispherically symmetric precipitation variability. *Quart. J. Roy. Meteor. Soc.*, **131**, 1501–1527.
- Shapiro, M. A., H. Wernli, N. A. Bond, and R. Langland, 2001: The influence of the 1997–99 El Niño Southern Oscillation on extratropical baroclinic life cycles over the eastern North Pacific. *Quart. J. Roy. Meteor. Soc.*, **127**, 331–342.
- Strong, C., and G. Magnusdottir, 2008: Tropospheric Rossby wave breaking and the NAO/NAM. *J. Atmos. Sci.*, **65**, 2861–2876.
- Thompson, D. W. J., and S. Solomon, 2002: Interpretation of recent Southern Hemisphere climate change. *Science*, **296**, 895–899.
- Thorncroft, C. D., B. J. Hoskins, and M. F. McIntyre, 1993: Two paradigms of baroclinic-wave life-cycle behaviour. *Quart. J. Roy. Meteor. Soc.*, **119**, 17–55.
- Trenberth, K. E., 1991: Storm tracks in the Southern Hemisphere. *J. Atmos. Sci.*, **48**, 2159–2178.
- Woollings, T., B. Hoskins, M. Blackburn, and P. Berrisford, 2008: A new Rossby wave–breaking interpretation of the North Atlantic Oscillation. *J. Atmos. Sci.*, **65**, 609–626.